

Mapping evapotranspiration variability over a complex oasis-desert ecosystem based on automated calibration of Landsat 7 ETM+ data in SEBAL

Friday Uchenna Ochege, Geping Luo, Michael Chukwuma Obeta, George Owusu, Eldiir Duulatov, Liangzhong Cao & Jean Baptiste Nsengiyumva

To cite this article: Friday Uchenna Ochege, Geping Luo, Michael Chukwuma Obeta, George Owusu, Eldiir Duulatov, Liangzhong Cao & Jean Baptiste Nsengiyumva (2019): Mapping evapotranspiration variability over a complex oasis-desert ecosystem based on automated calibration of Landsat 7 ETM+ data in SEBAL, GIScience & Remote Sensing, DOI: [10.1080/15481603.2019.1643531](https://doi.org/10.1080/15481603.2019.1643531)

To link to this article: <https://doi.org/10.1080/15481603.2019.1643531>



Published online: 16 Jul 2019.



Submit your article to this journal [↗](#)









Article views: 114



View Crossmark data [↗](#)

Mapping evapotranspiration variability over a complex oasis-desert ecosystem based on automated calibration of Landsat 7 ETM+ data in SEBAL

Friday Uchenna Ochege ^{a,b,c,d}, Geping Luo ^{*a,b,c}, Michael Chukwuma Obeta^e, George Owusu ^f, Eldiiar Duulatov ^{a,b}, Liangzhong Cao ^{a,b} and Jean Baptiste Nsengiyumva ^{a,b}

^aState Key Laboratory of Desert and Oasis Ecology, Xinjiang Institute of Ecology and Geography, Chinese Academy of Sciences, Urumqi, China; ^bUniversity of Chinese Academy of Sciences, Beijing, China; ^cResearch Center for Ecology and Environment of Central Asia, Chinese Academy of Sciences, Urumqi, China; ^dDepartment of Geography and Environmental Management, University of Port Harcourt, Port Harcourt, Nigeria; ^eHydrology and Water Resources Unit, Department of Geography, University of Nigeria, Nsukka, Nigeria; ^fDepartment of Geography and Resource Development, University of Ghana, Accra, Ghana

(Received 21 February 2019; accepted 10 July 2019)

Fragmented ecosystems of the desiccated Aral Sea seek answers to the profound local hydrologically- and water-related problems. Particularly, in the Small Aral Sea Basin (SASB), these problems are associated with low precipitation, increased temperature, land use and evapotranspiration (ET) changes. Here, the utility of high-resolution satellite dataset is employed to model the growing season dynamic of near-surface fluxes controlled by the advective effects of desert and oasis ecosystems in the SASB. This study adapted and applied the sensible heat flux calibration mechanism of Surface Energy Balance Algorithm for Land (SEBAL) to 16 clear-sky Landsat 7 ETM+ dataset, following a guided automatic pixels search from surface temperature T_s and Normalized Difference Vegetation Index NDVI ($T_{s_{hot}/NDVI}$, $T_{s_{cold}/NDVI}$). Results were comprehensively validated with flux components and actual ET (ET_a) outputs of Eddy Covariance (EC) and Meteorological Station (KZL) observations located in the desert and oasis, respectively. Compared with the original SEBAL, a noteworthy enhancement of flux estimations was achieved as follows: – desert ecosystem $ET_a \rightarrow R^2 = 0.94$; oasis ecosystem $ET_a \rightarrow R^2 = 0.98$ ($P < 0.05$). The improvement uncovered the exact land use contributions to ET_a variability, with average estimates ranging from 1.24 mm d^{-1} to 6.98 mm d^{-1} . Additionally, instantaneous ET to NDVI (ET_{ins} -NDVI) ratio indicated that desert and oasis consumptive water use vary significantly with time of the season. This study indicates the possibility of continuous daily ET monitoring with considerable implications for improving water resources decision support over complex data-scarce drylands.

Keywords: evapotranspiration; Landsat 7 ETM+; SEBAL; Small Aral Sea Basin-SASB; oasis-desert ecosystem

1. Introduction

The effective thermal vapor flux-induced processes in the atmosphere often influence the dominant water and heat budgets in drylands. Generally, this mechanism is controlled by evapotranspiration (ET) dynamics, a key operational component of the mass-energy transfer.

*Corresponding author. Geping Luo Email: luogp@ms.xjb.ac.cn

ET effects account for the over 65% of the precipitation that disappears into the atmosphere and reaches up to 90% in drylands where water scarcity recurrently threatens agricultural productivity (Kong et al. 2018; Yan et al. 2018). Moreover, climate variability, such as extreme temperature anomaly often intensifies the ET effects. Because ET is directly related to temperature trends and other complex factors that are anthropogenically induced, including urbanization (Wang et al. 2016; Jiang and Weng 2017; Nistor et al. 2017). Therefore, it is imperative to account for both past and present landscape evaporative demand, which is essential for ecosystem improvement, agrometeorological services and for developing efficient water management strategies (Yang et al. 2014). Nevertheless, due to regional inhomogeneity, the accurate estimation of actual ET (ET_a) is considered a challenging task, particularly in data-scarce regions burdened with little or no regular weather observations. For instance, the Small Aral Sea basin (SASB) is made up of several fragmented ecosystems. The SASB falls short of regular ET information due to sparse long-term ground-based weather observations. Moreover, field-scale ET methods that use weather station data are spatially insufficient to precisely account for regional ET estimates; thereby constraining the direct and continuous measurement of ET_a in the area.

Notwithstanding the constraints posed by the paucity of ground-based weather observations in arid Central Asia, ET_a information is continuously being required for efficient management of water resources for agrometeorological services and policy formulation. This is because of the shrinking of the Aral Sea (AS), which is a well-known crisis. The problem resulted in lake disintegration that left its fragments at risk of environmental vulnerability, including increasing temperature, anthropogenically induced oasis expansions, desertification and cropland abandonment (Micklin, Aladin, and Plotnikov 2014; Micklin 2016; Singh et al. 2018). On top of that, climate anomalies continue to cause alterations of land surface processes and anomalous change in the albedo, which affects the surface radiation balance (Meng et al. 2017). Signifying that, surface temperature (T_s) is a crucial variable in the estimation of ET and surface moisture (Jiang and Weng 2017). The situation is typical of the oasis-desert ecosystem, and particularly critical of inland watersheds, where changes in T_s respond inversely to the advective effect of surface fluxes controlled by the region's high evaporative fractions (Song et al. 2016). Unfortunately, not so much is known about oasis-desert effects on near-surface and vapor fluxes, notably, the contributions of different land use to ET_a changes in the SASB.

Some studies have reported on the evolving effect of oases-desert interactions, but have mostly focused on upper atmospheric circulation impacts using regional/global circulation models (Li et al. 2011b; Zhang et al. 2017). Singh et al. (2018) studied the shrinking South Aral Sea using datasets from spaceborne missions and reported on the inconsistency and underestimation of ET by altimetry observation and the MOD16 global ET project, respectively. Likewise, Conrad et al. (2007) employed a surface energy balance (SEB) algorithm to examine crop-water usage in Central Asia using coarse resolution data. However, no specific information on near-surface and vapor fluxes exist for the fragmented north Aral Sea, its basin landscapes, or its interface between lake-oasis-desert ecosystems. There is a need to improve our knowledge of these issues.

Here, we employed an effective way to estimate ET_a accurately, given that Remote Sensing (RS) offers a set of robust computational algorithms, with decades of reliable evidence in deriving ET distribution across space (Gowda et al. 2008; Karimi and Bastiaanssen 2015; Sur et al. 2015). Various kinds of remote sensing of ET algorithms and their advancements towards accurate prediction and up-scaling of

ET estimates have been recognized (Wang and Dickinson 2012). The Surface Energy Balance Algorithm for Land (SEBAL) (Bastiaanssen, Menenti, and Holtslag 1998a) has consistently been applied to different climatic zones and has demonstrated exceedingly reliable (Mutiga, Su, and Woldai 2010; Lee and Kim 2016; Yang et al. 2018). In recent times, the calibration and application processes of SEBAL and its variant – METRIC (Mapping EvapoTranspiration at High Resolution with Internalized Calibration) can be highly automated (Biggs, Marshall, and Messina 2016; Bhattarai et al. 2017, 2019). Such that development of improved ET model optimization frameworks and robust RS tools raises the awareness of their capabilities to rapidly overcome the tedious practical constraints in endmember pixel selection required for model calibration, even in heterogeneous regions (see, for example, Owusu 2017; Bhattarai and Liu 2019; Jaafar and Ahmad 2019). When integrated with *in situ* climatic data, SEBAL can effectively partition available surface energy, from which evaporative fractions required for obtaining ET_a estimates are derived (Bastiaanssen, Menenti, and Holtslag 1998a; Bastiaanssen et al. 1998b; Allen et al. 2011). Also, with high-resolution datasets, such as the ASTER (15 m, 16-day) and Landsat (30 m, 60 m, 16-day) products, SEBAL can upscale the satellite overpass time instantaneous evaporative fraction to daily, seasonal or annual ET_a estimates (Hong, Hendrickx, and Borchers 2009; Grosso et al. 2018; Yang et al. 2018).

The skill of SEBAL includes the computation of ET_a at each pixel, and over large areas with minimal *in situ* data, especially where ground measurements are unavailable. Further details of SEBAL, its improvements and evaluation have been extensively documented (Bhattarai et al. 2017; Biggs, Marshall, and Messina 2016; Kong et al. 2018; Long and Singh 2010; Wang and Dickinson 2012; Karimi and Bastiaanssen 2015). Generally, the accuracy level of SEBAL as shown in previous studies indicate that it is a robust tool for mapping ET_a at varying spatiotemporal scales and is very effective for, at least, one growing season ET estimation (Allen et al. 2001, 2011; Grosso et al. 2018; Gowda et al. 2008). Above all, SEBAL has high potentiality for excellent predictions for arid and semi-arid regions (see, for example, Bastiaanssen et al. 2005; Yang et al. 2018; Al Zayed et al. 2016).

Errors in SEBAL model calibration can be reduced through careful manual or automated end member pixel selection required for model parametrization, improved iteration of model implementation, especially, over highly heterogeneous terrains (Timmermans et al. 2007). The improved end member pixels selection is not entirely new in the use of SEB to estimate ET. Most researchers tend to use different input variables, and or selection criteria that are based on random pixel search due to regional variability (Choi et al. 2009; Biggs, Marshall, and Messina 2016; Bhattarai et al. 2017). Likewise, others have based their evaluation on the expert calibrated pixels of Albedo (α) and Normalized Difference Vegetation Index (NDVI) (Silva Oliveira et al. 2018) and T_s (Lee and Kim 2016) with the pixel of the same variable used for calibrating the SEB models. This study purposefully validated ET produced from the automated calibration with the SEBAL model calibration-based ET estimates for the SASB. So, the automatic pixel selection may be considered a domain-specific approach that helps reduce uncertainty, saves time and optimize ET simulations beyond research purposes.

Therefore, as a contributive effort in the study area, the aim here is to assess the robustness of the SEBAL model to generate ET information for a region with high potential for agrometeorological services, yet, less of ground-based observations. Moreover, a growing season ET response to canopy density and water stress conditions in the

ecosystems were examined. The specific objectives include: (1) the estimation of near-surface fluxes and ET_a using both the original and automatically calibrated SEBAL; (2) accuracy evaluation of the near-surface fluxes and ET_a outputs with available ground-based observations; (3) the quantification of a growing season contribution to ET_a variability in the oasis and desert ecosystems.

2. Material and methods

2.1 Study area

SASB is situated within fragmented ecosystems of the desiccated Aral Sea (Lat. 45.04° to 47.01°N and Long. 59.97° to 63.08°E). The basin consists of an inland lake, an evolving oasis-desert ecosystem, and is traversed by the delta of Syr Darya River which supports the expansion of the oasis (Figure 1). The climate is arid and continental. Average lowest temperatures fluctuate between -1.4°C and 4°C (late August-February), while highest temperatures ($\sim 30^{\circ}\text{C}$) are experienced in July-early August (Kostianoy and Kosarev 2010). Annual precipitation ranges between 125 mm – 160 mm, while net average evaporation is 960 mm – 1546 mm (Li et al. 2011a; Micklin, Aladin, and Plotnikov 2014). Height of the study validation sites ranges between 50–75 m a.s.l. The area is drained by the Syr Darya River, a snowmelt-dominated basin with scarce hydrological stations and ground observation data. This river originates from the Tianshan mountains and empties in the Small Aral Sea (SAS). However, the water budget of SAS became unstable after 1960 due to the intensive unsustainable distribution of river runoff to increase irrigation farming, which contributes to its gradual shrinkage (Kostianoy and Kosarev 2010). The decline in the average discharge into the SAS from river runoff (from 8.5Km^3 in 1994 to $5\text{--}6\text{ km}^3$ in 2014) made it possible to observe net water outflow, which is about 2 to 3 km^3 (Micklin, Aladin, and Plotnikov 2014). This has dramatically impacted the surrounding oasis-desert environment such that, as heating of surface water progressed, sea surface salinity grows with distance from the river mouths where it was low; and then between July and August, a halocline tends to form in the surface layer which coincides with the thermocline to intercept vertical mixing (Kostianoy and Kosarev 2010). This mechanism indirectly increases the lake evaporation rates, likewise ET within the surrounding oasis-desert ecosystem.

2.2 Data and preprocessing

2.2.1 Land use cover

A suitable reference landcover product, originally classified into 24 categories, was accessed for this study. Through field validation using existing topographic sheets (1:1,000,000) and total station GPS, high-resolution (30 m) land use land cover (LULC) maps for different years, including 2012, were generated by the Remote Sensing and GIS application Laboratory of Xinjiang Institute of Ecology and Geography (XIEG), Chinese Academy of Sciences (Figure 1b). The 2012 land use land cover map maintains a ranked classification structure, which includes 6 classes and 25 subclasses. This map has been effectively used in other studies (For example, Zhang et al. 2017). Based on the United States Geological Survey (USGS) classification, we reclassified the 2012 LULC map into five classes, following oasis-desert cover types in the study area. The classes are oasis (irrigated farmlands), oasis (non-irrigated and arable fallow land), desert (bare surfaces and

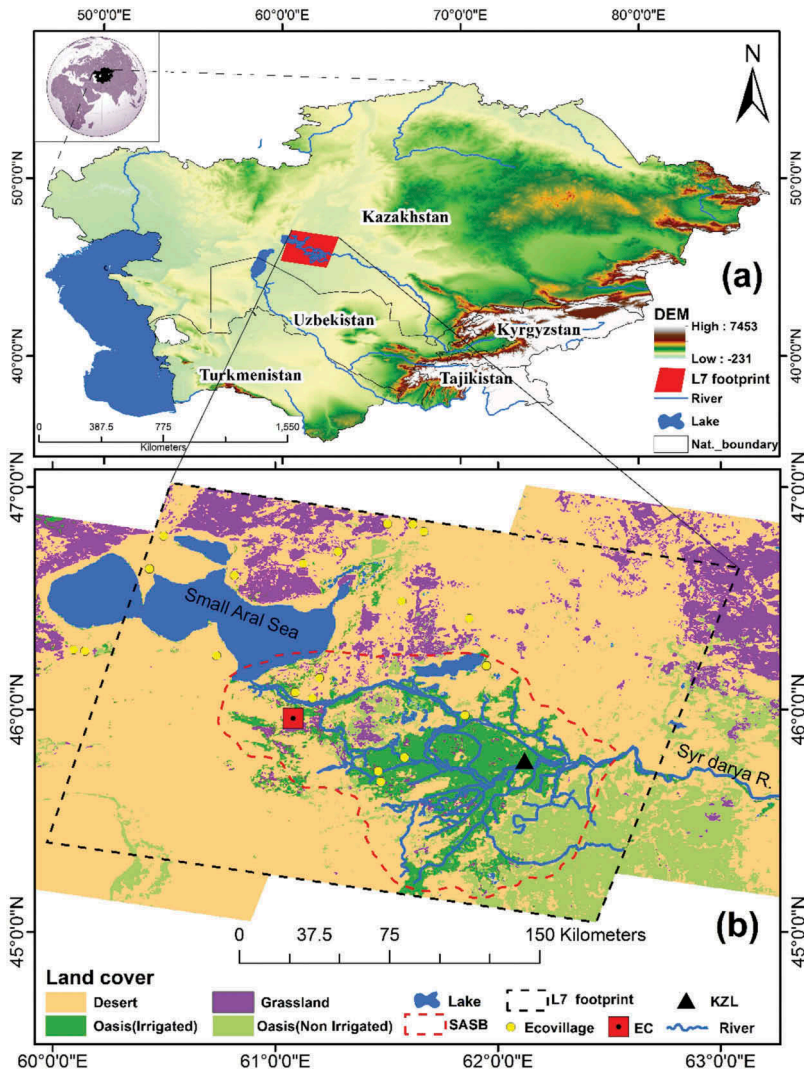


Figure 1. (a) Digital elevation model of Central Asia acquired by Shuttle Radar Topography Mission; (b) Landsat 7 ETM + footprint of 2012 land cover marked by black dotted lines, and showing validation sites within the small Aral Sea Basin as indicated by the red dotted lines. The Delta-dominated oasis with patches of desert grassland is well-drained by the river Syr Darya tributaries traversing the SASB. Basin size ET maps were produced from the automated SEBAL modeled ET_a . However, land use ET_a and ET_{ins} -NDVI ratio estimates were extracted from within 450 m^2 of each validation station fetch area. The Eddy Covariance-EC flux station (red dot) (situated in desert-grassland, within the basin) and KZL meteorological station (situated in the oasis, within the basin) were the exact locations used for energy flux components (EC) and KZL site ET_a validations.

sand), grasslands (desert-grasslands) and water bodies (rivers, lakes, wetlands) (Figure 1b). The new landcover map was used to mask out the various land cover ET_a in order to determine basin landscape evaporative demand within the oasis and desert ecosystems.

2.2.2 Landsat 7 ETM +

This study utilized 16 high-resolution Landsat 7 ETM + (GeoTIFF) images, made available by USGS at no cost. The ETM+ instrument has a 16 days revisit with a scene coverage of 185 km x 170 km. The spatial resolution on the visible bands is 30 × 30 m, while the thermal bands are 60 × 60 m. The thermal bands were resampled into 30 m for distribution purposes. Through established ground control points (GCPs), the Landsat 7 ETM+ datasets were terrain-corrected to provide high radiometric and geometric accuracy. However, since our study area required, at least, a full scene coverage to capture experiment sites (Figure 1), the SLC-off (scan line corrector off) scenes had to be corrected with the focal analysis technique. The ETM+ sensor is an improved instrument that guarantees a better-quality geometric calibration accuracy, reduced noise and reliable spectral information. With these features, confidence is built that mapping ET with Landsat 7 ETM + provides accurate estimates. Details are presented in Table 1.

The obtained images were of clear-sky, representing various days of the year (DOY) spanning through the growing season of 2012–02 April to 27 October. All the 16 images fall on the same row (028), but different paths (159,160,161). The adjacent image scene paths 159 (1 image) and 161 (5 images) to the scene on the centre of the study site (160) were merged and cropped to ensure spatially precise ET estimates, reduce uncertainty in monthly ET estimates and seasonal effects. The advantage is, considering the ETM+ sensor revisit time (16-day), there was the possibility to generate accurate ET estimates that are reliable given the potential provision of more images within a month. The satellite overpass time of each image, at their exact local time was put to consideration in the model calibration (Table 1). To generate SEBAL input variables (surface albedo and emissivity – α , vegetation and soil indices – NDVI, Leaf Area Index (LAI), Soil Adjusted Vegetation Index (SAVI), surface emissivity – ϵ , and surface temperature – T_s), the spectral radiance ($L_\lambda, Wm^{-2}sr \mu m$) and reflectivity ($\rho_\lambda, Wm^{-2}sr \mu m$) were computed using the calibration coefficient from the Landsat 7 ETM+ image visible bands (1–5, 7) and the thermal band (6) as elucidated in (Allen et al. 2002; Landsat Handbook 2007) and with the following equations:

$$L_\lambda = (\text{Gain} \times \text{DN}) + \text{Bias} \quad (1)$$

$$\rho_\lambda = \frac{\pi \times L_\lambda}{\text{ESUN}_\lambda \times \cos\theta_s \times d_r} \quad (2)$$

$$T_s = \frac{K_2}{\ln\left(\frac{\epsilon_{NB} K_1}{K_1}\right) + 1} \quad (3)$$

Where, DN stands for digital number, ESUN_λ represents average solar exoatmospheric irradiance ($Wm^{-2}sr \mu m$), and θ represents solar angle of occurrence at $90^\circ - \beta$ which is the angle of solar elevation. The inverse form of sun relative distance of the earth is denoted by d_r , while K_1 and K_2 equals 666.09, 1282.71, respectively (Allen et al. 2002). T_s was retrieved from thermal band with high gain; then, the ratio of the reflected radiation flux was converted to surface reflectance. Also, because NDVI has proven

Table 1. Details of satellite products, flux and ground-based weather observation.

Data type/ Instrument	Date (2012 growing season DOY)/measurement	Footprint/ Location/ Altitude	Satellite Overpass (GMT)	Local Time (UTM+5)/LULC
Landsat 7 ETM +	2 April 2018 April, 4 May 2020 May, 5 June 2028 June, 12 June, 7 July 2014 July, 23 July 2015 Aug., 31 Aug., 2 Sept., 25 Sept., 11 Oct., 27 Oct.	159/028, 160/028 161/028, 30 m Resolution	06:34:41, 06:34:40, 06:35:07, 06:35:16, 06:34:54, 06:41:10, 06:41:18, 06:35:16, 06:41:32, 06:35:27, 06:41:54, 06:42:04, 06:29:44, 06:36:08, 06:36:15, 06:36:25	11:34:41, 11:34:40, 11:35:07, 11:35:16, 11:34:54, 11:41:10, 11:41:18, 11:35:16, 11:41:32, 11:35:27, 11:41:54, 11:42:04, 11:29:44, 11:36:08, 11:36:15, 11:36:25
XIEG, Chinese Academy of Sciences	2012 LULC: 24 major categories, with 16 and 12 subcategories (12 for the study area before reclassification).	Landsat footprint (160/028) and Clipped Extent 30 m Resolution	Data User Element – 2012 Regional land Cover	Reclassified Land cover types include Oasis (irrigated and no-irrigated), grassland, desert, water, and others.
Eddy covariance flux tower at Kzara-Ara (EC)	Fluxes of net radiation (Rn), soil heat (G), sensible heat (H) and latent heat (LE) (Wm^{-2}) and other climate data	61°4'48"E, 45°57'36"N, Alt. = 52 a.s.l. (~450 m)	April – August, 2012	Land cover type includes desert grassland, shrub, patches of the irrigated and non- irrigated oasis, and the lake water and bare surfaces.
Meteorological station at Kazalinsk (KZL)	Climate data: relative humidity (%), minimum, maximum, mean air temperature ($^{\circ}\text{C}$), R_n (Wm^{-2}), sunshine hours, wind speed (ms^{-1}), and minimal rainfall data (mm).	62°9'36"E, 45°46'12"N, Alt. = 66 m a.s.l.	January – December 2012	Expanding oasis, dominated by irrigated arable land, rice fields, non-irrigated and the river Syr Darya delta, patches of desert grasslands.

a satisfactory indicator in detecting inherent land use consumptive water use and canopy conductance (Gao et al. 2014; Gong et al. 2017; Boegh et al. 1999), the automatically calibrated NDVI and ET_{ins} were evaluated to show underlying evaporative demand of oasis-desert ecosystem during the growing season (Section 3.5).

2.2.3 Meteorological observation and actual ET measurements

ET was measured by using data obtained from an Eddy Covariance system (EC) and a meteorological (KZL) Station (Table 1). The EC system was installed on April 2012 in desert grassland, 23 km from the nearest coast of the SAS and 10 km from the nearest ecovillage – Zhanakurylys. It monitored energy fluxes, momentum, CO_2 and H_2O . A 10 Hz quick response sonic anemometer-3D was attached 2 m high to record mean quantities of vertically and laterally fluctuating wind speed and air temperature values. During the period of observation, the head of the sonic anemometer often pointed northeast following the prevailing wind direction, with ranges from 0.1–11.8 $m\ s^{-1}$. Based on this, with consideration of the height of equipment at zero-plane displacement and height of canopy (1/2 m), the flux fetch area was determined (~ 450 m). Previous studies considered slightly larger than this footprint for mapping and validating near-surface vapor fluxes (Jiménez Bello et al. 2015; Madugundu et al. 2017). Other measurements recorded include, precipitation, humidity, downwelling and upwelling shortwave and longwave radiation and flux density of photosynthetically active radiation (PAR). Also, the EC system was calibrated to measure G, soil moisture content at depths of 0.20, 0.40, 0.60 and 0.80 m. A half-hourly data logger (CR500, Campbell Sci. Inc., Logan, UT) was installed to automatically store (10 Hz) all the readings (averages) in *.ghg file format (Li et al. 2014). Additional climate information was accessed from the Kazalinks meteorological station (KZL) (Table 1). The KZL station was not calibrated to observe energy flux components of ground heat, sensible heat and latent heat (G, H, and LE). A sensitivity analysis, involving correction of energy balance misclosure was performed on the measured flux elements (R_n , G, H, and LE), using the energy balance closure ratio $EBR = [(LE + H)/(R_n - G_{soil})]$. Figure 2 shows the coefficient of determination ($R^2 = 0.92$), reasonable slope (0.77) and intercept (44.18 $W\ m^{-2}$) for half-hourly energy balance closure for the growing season of 2012, indicating a strong correlation of turbulent sensible heat to available energy at the EC station.

These data sets are considered the explanatory variables to ET. Therefore, they served as ancillary inputs for SEBAL implementation and apportioning of the surface energy budget. Then, following equation (4), at every half-hour, energy balance residual was derived and transformed using vaporized water constant (2.45 $MJ\ mm^{-1}$) to divide LE ($MJ\ m^{-2}$ per half hour) (Allen et al. 2006; He et al. 2017). From these estimates, daily and monthly ET distribution were derived for all land cover types, including the water bodies. The daily and cumulative monthly ET estimates were used for SEBAL validation and mapping season distribution of ET_a across the oasis-desert ecosystem.

2.3 SEBAL, adjustment and implementation for actual ET measurements

The theory and formulation of the SEBAL model have already been elaborated and is extensively documented (Bastiaanssen, Menenti, and Holtslag 1998a; Timmermans et al. 2007; Allen et al. 2011). It requires a skilful identification and selection of cold surface and dry surface pixels; for the computation of instantaneous net radiation, soil heat and sensible heat fluxes from which λET – Evapotranspiration is derived, as expressed in equation 4:

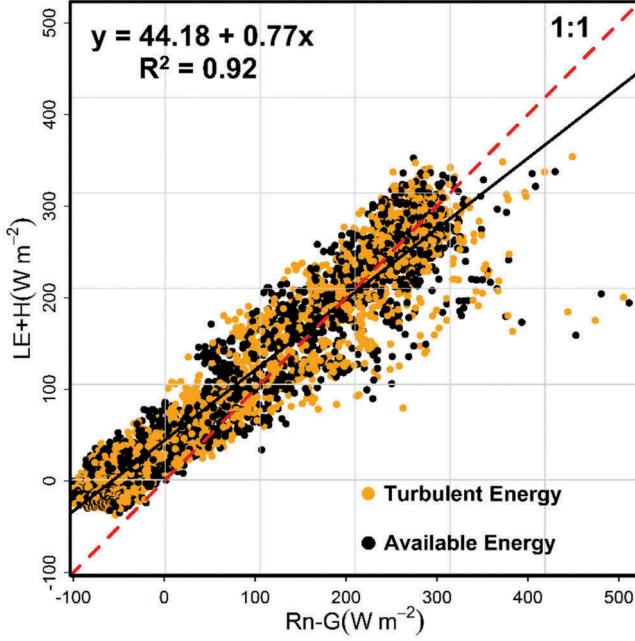


Figure 2. Turbulent heat flux relationship with available energy at the EC station. (The 1:1 red dotted line indicates a reasonable agreement based on the fitting linear model).

$$\lambda ET \equiv LE = R_n - G - H \quad (4)$$

The coefficient of LE of vaporization ($\sim \text{J kg}^{-2}$) is denoted by λ . The expression of ET is in mm, while all the four flux components $-LE, H, G, R_n$ are in W m^{-2} . These variables then serve as inputs used by land surface energy balance models to accurately compute ET_a from the evaporative fraction [$\lambda ET / (R_n - G)$] (Bastiaanssen et al. 2005) after partitioning the major energy components following eqns. 5–8:

$$R_n = (1 - \alpha)S_{\downarrow} + (L_{\downarrow} - L_{\uparrow}) - (1 - \varepsilon)L_{\downarrow} \quad (5)$$

$$S_{\downarrow} = G_{sc} \times \cos \theta \times d_r \times \tau_{sw} \quad (6)$$

$$L_{\downarrow} = 1.08(-\ln(\tau_{sw}))^{0.265} \times \sigma T_a^4 \quad (7)$$

$$L_{\uparrow} = \varepsilon \sigma T_s^4 \quad (8)$$

where $\alpha, \varepsilon, L_{\downarrow}, L_{\uparrow}, S_{\downarrow}$ represent surface albedo, surface emissivity, downward longwave radiation (Wm^{-2}), ascending longwave radiation (Wm^{-2}), and descending shortwave radiation (Wm^{-2}), respectively. The solar constant $G_{sc} = 1367(\text{Wm}^{-2})$, τ_{sw} represent the single pathway transmissivity [$\tau_{sw} = 0.75 + 2 + 10^{-5} \times Z$ (a.s.l.)], $\sigma = 5.67 \times 10^{-8} \text{Wm}^{-2} \text{K}^{-4}$ (Stefan-Boltzmann constant), and T_a represent air temperature at the meteorological sites. Here, the parameterization scheme of S_{\downarrow} accounts for the entire oasis-desert ecosystem in this study because the incident of shortwave

fluctuates disproportionately with topography such as water level and land surface azimuth (Long and Singh 2010). In sparse vegetation, soil evaporation plays a crucial role in total ET_a for desert surfaces and watered bodies. As such, SEBAL considers water-heat exchange from G as a part of R_n , such that the estimated fragment is the inverse of the albedo, T_s and NDVI for vegetation surface, using equation 9:

$$G = R_n(0.0038 + 0.0074\alpha)(T_s - 273.15)(1 - 0.98NDVI^4) \quad (9)$$

Where T_s is expressed in °C and $NDVI$ is the variance between the red and near infrared bands of Landsat 7 ETM+. Therefore, to reduce uncertainty, we adjusted the endmember pixels for SEBAL calibration through a guided automated in-depth search, as against the manual random selection of representative pixel candidates, used for investigating the advection effect of oasis-desert ecosystem ET_a in one growing season. Unlike in the original SEBAL, coldandhotpixelsselection used for computing H in this study was driven by automatic computation of radiometric surface temperature based on NDVI, T_s and or albedo, under clear sky condition. Specifically, cold pixels, represented by T_s [Cold/Wet]/NDVI surface portion of the Syr Darya delta (about 5% of the Landsat clipped portion) were sorted out from the most lush, well-watered irrigated surface around the KZL station. The hot pixels, represented by T_s [hot]/NDVI (about 15 to 20% of the clipped portion) were selected from desert and desert grassland cover around the EC station. Note that the hot pixel selection was dependent on the particular day of the season, because of the low NDVI rates associated with dry surfaces despite their high T_s (Figure 3).

The period of investigation hardly experienced rainfall, so, representative T_s of hot pixels were regularly adjusted during the calibration process, especially in the peak of summer (late June to late July). This helped to reduce the uncertainty associated with variations in vegetation wetness, stomatal conductance or intrinsic error variance in image digital numbers. Lastly, a guided visual inspection of selected candidates was carried out after each automation to ensure that selected pixels correctly fall within the appropriate land cover types. This criterion conforms with the selection procedure prescribed for METRIC, which maintains a similar

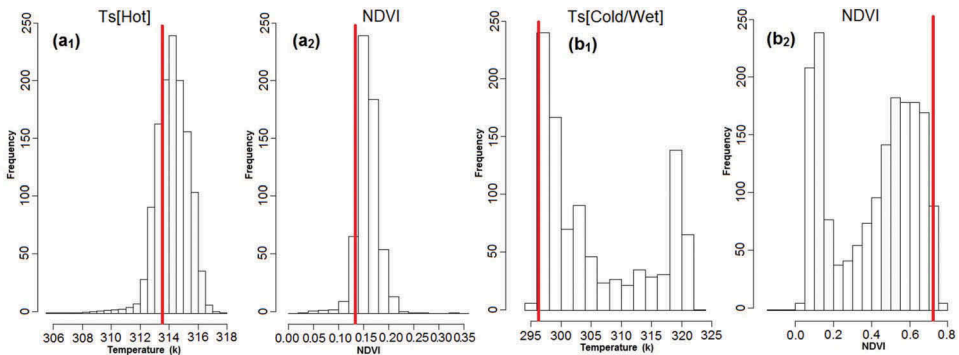


Figure 3. Improved performance of frequency distribution histograms showing automatic pixels selection of (a₁) T_s [hot] pixels, (a₂) NDVI [dry] pixels, and (b₂) T_s [cold] pixels and (b₂) NDVI [wet] pixels. Figure 3 (a₁ and a₂) represents an ideal selection in desert grassland, while (b₁ and b₂) is a representation for pixel selection in the oasis (irrigated arable land) within the Syr Darya delta, indicating improved model calibration.

parameterization scheme with SEBAL (Allen et al. 2013). However, following the original SEBAL formulation (Bastiaanssen, Menenti, and Holtslag 1998a), the manual pixel selection was carried out to validate the automated pixel calibration. These pixels were identified manually based on expert judgement on the image (Bastiaanssen et al. 2005). For our study area, hottest pixels are located in the bare surfaces of dried desert grassland while the cold surface pixels were identified from the irrigated oasis and arable lands – wet surfaces. Thus, a_0 and b_0 were calculated as follows (equ. 10–11):

$$a_0 = \frac{r_{ah_hot}}{\rho_{hot} c_p} \times \frac{R_{n_hot} - G_{hot}}{T_{s_{hot}/NDVI} - T_{s_{cold}/NDVI}} \quad (10)$$

$$b_0 = \frac{r_{ah_hot}}{\rho_{hot} \times c_p} \times \frac{(R_{n_hot} - G_{hot}) T_{s_cold}}{T_{s_{hot}/NDVI} - T_{s_{cold}/NDVI}} \quad (11)$$

where r_{ah_hot} , ρ_{hot} , R_{n_hot} and G_{hot} , represent heat transfer arising from aerodynamic resistance from the pixel with driest surface, air density from pixel with driest surface, the instantaneous R_n and G fluxes for the driest pixels, respectively. The linear regression coefficients are represented by a_0 and b_0 . $T_{s_{hot}/NDVI}$ and $T_{s_{cold}/NDVI}$ signify pixels with the driest and wettest land surface temperature. Then, the convergence of a_0 and b_0 was reached after repeated iteration before calculating H . The complication with H lies with dT and r_{ah} , in that both are initially unknown. Therefore, an iterative parameterization procedure based on the Monnin-Obukhov Similarity formulation (Brutsaert 1999) was applied concurrently to equations 12–13. In this way, the assumption that dT is linearly related with T_s (Bastiaanssen, Menenti, and Holtslag 1998a) is clarified, as automated coefficients a_0 and b_0 were used to drive the iterative process after dT was approximated for each pixel of the clipped Landsat 7 ETM+ images, based on a direct relationship between dT and T_s , i.e., $dT = a_0 + b_0 \times T_s$. Therefore, calculating H in the form (Equ. 12–14) explains the updraft across the different surfaces and to neutralize any unavailable surface resistance mechanism (e.g., aerodynamic temperature) associated with the original model framework.

$$H = \rho c_p \frac{dT}{r_{ah}} = \frac{(a_0 T_s + b_0)}{r_{ah}} \quad (12)$$

$$u^* = \frac{ku_{200}}{\left[\ln \left(\frac{200}{Z_{0m}} \right) - \psi_m - Z_{(200)} \right]} \quad (13)$$

$$r_{ah} = \frac{1}{ku^*} \left[\ln \left(\frac{Z_2}{Z_1} \right) - \psi_{h(Z_2)} + \psi_{h(Z_1)} \right] \quad (14)$$

Where ρ is the density of air (Kgm^{-3}), c_p represent the definite heat capacity of air at a pressure constant of $1004 \text{JKg}^{-1} \text{K}^{-1}$, dT denote altitudinal surface temperature variations amongst $[Z_1(0.1\text{m}) \text{ and } Z_2(2\text{m})]$. Frictional velocity and Von Karman's constant are

denoted by u^* (ms^{-1}) $K(0.41)$; while the improvement factors of momentum and sensible heat transfer are represented by ψ_m and ψ_h , respectively (Long and Singh 2010). Then, Instantaneous ET , signified by the ratio of LE flux is then made available [$\lambda E/(R_n - G)$]. It is assumed constant throughout the day, and was then derived and transformed ($W m^{-2}$ to $mm d^{-1}$) based on equation 15:

$$ET_{24_SEBAL} = (86,400 \times EF_{ins} \times R_{n24})/\lambda_v \quad (15)$$

where daily ET is ET_{24} , and 86,400 is time conversion of seconds in a day. The day-to-day LE of vaporization (λ_v) is computed as a mean of daily air temperature. Given that daily net radiation (R_{n24}) is the main variable used for estimating the magnitude of ET , season ET was estimated from the day-to-day ET output of SEBAL following equation 16:

$$ET_{24_period} = \sum_{i=m}^n [(EF_{ins}) \times (ET_{r_period})] \quad (16)$$

where EF_{ins} is the daily instantaneous evaporative fraction of period i , ET_{r_period} is the reference ET_{r_period} (i.e., ET_o or ET_r) representing the overall ET_r from the observation for the understudied period m to n (Allen *et al.* 2002). So, season ET_a (ET_{24_period}) was derived by cumulatively adding daily ET_a grids of the growing season – April to October 2012 (Cuenca, Ciotti, and Hagimoto 2013; Al Zayed *et al.* 2016). SEBAL model implementation, which includes the initial Landsat 7 data preprocessing and iterative processes required for the derivation of energy flux components, model input variables and the automatic selection of “cold” and “hot” pixels were performed in RStudio software (R2018 Inc., Boston, MA, USA, 2015).

2.4 Data analysis and model validation

The SEBAL_{auto}-modeled surface and vapor fluxes estimates were evaluated with the ground-based measurements at each site using determination coefficient (R^2) and the trend line of the coefficient (slope). The Root Mean Square Error (RMSE), with the Mean Absolute Deviation (MAE), were statistically applied to determine the accuracy of the modeled land surface fluxes (Ortega-Farias and López-Olivari 2010). RMSE indicates the degree of error in the units of the observed and modeled constituents, where 0 indicates a perfect fit, while MAE determines the deviation of the prediction accuracy.

3. Results and discussion

3.1 Validation of energy flux components

The simulated instantaneous energy flux components estimated from both the SEBAL and SEBAL_{auto}-modeled fluxes, at the corresponding local time with satellite overpass, were linearly compared with EC flux estimates. Figure 4 shows the performance of the simulated parameters (R_n , G , H and LE) over the study sites. Most of the points on the scatter plots that fall above, and or, are distant from the threshold (1:1), show some form of overestimation. Also, this explains the uncertainty in that particular model performance, especially with (a, c) of the original SEBAL.

The comparison was done for the DOY matching with data availability. Therefore, it should be noted that the energy flux comparison was performed for only the EC flux station because the weather station was not calibrated to observe flux elements – G, HandLE. Due to the heterogeneity and arid nature of the sites, R_n was observed to range from 400 to 500 Wm^{-2} . This is a common phenomenon in most drylands, as some studies have reported R_n of over 500 Wm^{-2} in semi-arid and reaching 790 Wm^{-2} for arid land (Mira et al. 2016). Figure 4 presents a reasonably correlated output of all the flux components for the EC experiment site, as indicated by the red dotted 1:1 line. However, in comparison, some dissimilarities are revealed in the evaluation of some of the flux components, despite the high coefficients of determination obtained.

The R^2 for R_n was 0.95 for SEBAL compared to 0.89 of the SEBAL_{auto}-modeled R_n (Figure 4a and e). Likewise, the RMSE and MAE are 58.92 Wm^{-2} and 58.64 Wm^{-2} for SEBAL R_n , 8.10 Wm^{-2} and 6.87 Wm^{-2} for SEBAL_{auto}-modeled R_n . SEBAL overestimated R_n (50.82 m^{-2}) with a mean absolute deviation of 51.77 Wm^{-2} , as shown by 1:1 line in Figure 4(a). The disparities in estimated R_n by the original SEBAL can be simplified by overestimation in other flux components. Similarly, previous studies had reported that systematic overestimation, and or underestimation of heat fluxes can be associated with SEBAL when there is no distinct variation in T_s of dry and wet pixels surfaces of the understudied area (Kong et al. 2018; Tang et al. 2013). Hence, a justifiable reason for the model adjustment in this study. As evidenced in the model calibration output plot, T_s [hot] and NDVI pixels of DOY 180 receiving the highest R_n in the growing season (Figure 4), indicated the representing T_s [Hot] pixels with high albedo in summer of DOY 180 maintained a corresponding spatial variation with land cover with low NDVI of < 0.15 (Figure 4 (b₁)). Suggesting that the ratio of G to R_n vary disproportionately in terms of regional advection, and is capable of increasing latent heat by doubling the available energy (Allen et al. 2011). Given that R_n determines the availability of energy for other flux components and is the primary driver of ET, our study ensured that all the flux components were validated as a “proper ratio proportion” above the evaporative surface on cloud-free days to reduce uncertainty.

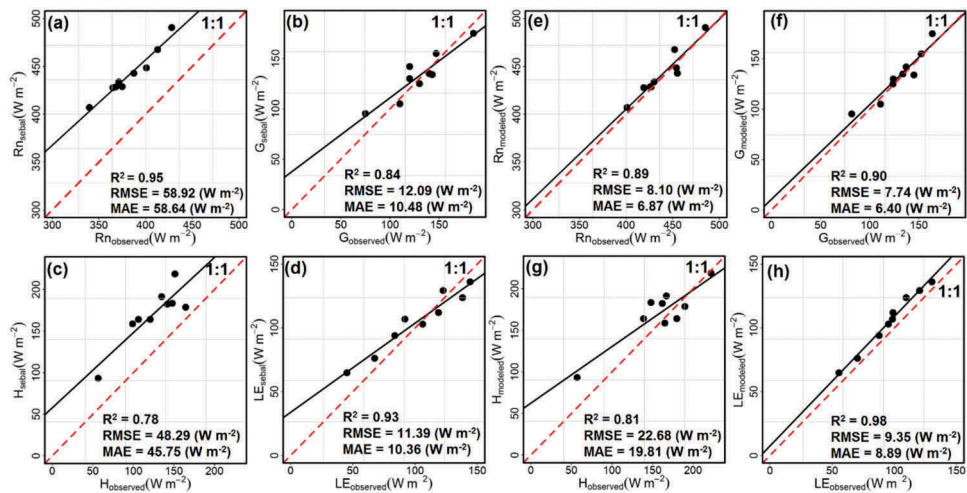


Figure 4. (a-d) Represent the relationship between original SEBAL and EC observed estimates, while (e-h) represent the SEBAL_{auto}-modeled fluxes against the EC observed estimates.

G is usually the smallest among all energy flux components, especially over bare desert surfaces (Cuenca, Ciotti, and Hagimoto 2013), however, may tend to return high estimated values. In our experiment, G range from 90 Wm^{-2} to 175 Wm^{-2} . The R^2 was 0.84 and 0.90 for original SEBAL and the SEBAL_{auto}-modeled G, with RMSE of 12.09 Wm^{-2} and 7.74 Wm^{-2} , respectively. Figure 4 (b and f) show that the mean absolute error difference was 4.08 Wm^{-2} . Not so much significant variation is shown between the SEBAL and SEBAL_{auto}-modeled G flux; however, the line of best fit clearly shows a reduced error with the SEBAL_{auto}-modeled G flux. This is revealed in the increased slope of 0.73 (SEBAL) to 0.94 (SEBAL_{auto}-modeled). Figure 4 (c and g) show that the R^2 for H is 0.78 and 0.81 for SEBAL and the SEBAL_{auto}-modeled, respectively. The RMSE of 48.29 Wm^{-2} for SEBAL, and 19.81 Wm^{-2} for the SEBAL_{auto}-modeled H, indicating an overestimation of H by 23.07 Wm^{-2} as revealed by the MAE and the 1:1 line. Table 2 presents the detailed statistics of evaluation for all flux components.

For SEBAL LE, measurements such as R^2 , RMSE and MAE are 0.93, 11.39 Wm^{-2} and 10.33 Wm^{-2} , respectively. The obtained values for the same measurement parameters for the SEBAL_{auto}-modeled LE are 0.98, 9.35 Wm^{-2} and 8.89 Wm^{-2} , respectively. These may suggest a near perfect correlation with the observed, however, SEBAL model deviation of 2.04 Wm^{-2} and prediction error of 1.44 Wm^{-2} was indicated, with a slope difference of 0.33 (Table 2). Most of the scatter in Figure 4 (d) did not fit perfectly as those in Figure 4 (h). Note that remote sensing surface energy balance LE estimation depends mostly on available energy and evaporative fraction. Therefore, the accurate estimation of SEBAL and the SEBAL_{auto}-modeled LE relied heavily on the accuracy of R_n which can be influenced by daytime insolation, air temperature, and probably surface emissivity (NDVI) (Allen et al. 2013). Based on the overall agreements and stability of the adjusted pixel selection, the SEBAL_{auto}-modeled SEBAL is more skilful at partitioning all energy flux components in the oasis-desert ecosystem.

Table 2. Performance of SEBAL_{auto}-modeled energy flux components as indicated by the coefficient of determination (R^2), slope, RMSE and MAE at the EC site.

Fluxes/ Parameters	SEBAL (W m^{-2})				SEBAL _{auto} -Modeled (W m^{-2})			
	R_n	G	H	LE	R_n	G	H	LE
R^2	0.95	0.84	0.78	0.93	0.89	0.90	0.81	0.98
RSME	58.91	12.09	48.29	11.39	8.10	7.74	19.81	9.35
MAE	58.64	10.48	45.75	10.33	6.87	6.42	22.68	8.89
Slope	0.89	0.73	0.90	0.69	0.94	0.94	0.93	1.02

Note that differences in computed and ground-observed sensible heat flux can be affected by weather variability at each time of the season of investigation, because saturated soil conditions can contribute to uncertainty in H. Also, it could arise from a limited range of T_s between hot and cold pixels used in the iterative computation of H (Cuenca, Ciotti, and Hagimoto 2013). However, as shown in the histograms of representative automated anchor pixels illustrated in Figure 3, which conforms with the general rule of pixel calibration – dry pixel from a dry surface and a wet pixel from irrigated or shallow water (Allen et al. 2013; Tang et al. 2013). Even, when the spatial scale effect about the domain size during pixel calibration is insignificant, the comparative scale of H can reduce uncertainty with LE. As seen in Figure 4 (d and h), the compared latent heat of SEBAL_{auto}-modeled and original SEBAL separately showed good agreement with EC system observation.

3.2 Validation of daily et_a estimates with the ground-based measurements

SEBAL_{auto}-modeled daily ET was validated by using the standardized EC and the meteorological station ET estimates (Figure 5).

In comparison, the SEBAL_{auto}-modeled ET significantly ($P < 0.05$) returned high precision values for desert and oasis as shown by the coefficient of determination (0.94 against 0.40, 0.98 against 0.88) with low model prediction accuracy values, based on RMSE (0.16 mm d⁻¹ against 0.48 mm d⁻¹, 0.38 mm d⁻¹ against 0.91 mm d⁻¹) and MAE (0.10 mm d⁻¹ against 0.35 mm d⁻¹, 0.28 mm d⁻¹ against 0.72 mm d⁻¹). Figure 6 shows the time scale of ET_a intra-season variability over the understudied growing season. A strong agreement is exhibited for the SEBAL_{auto}-modeled daily ET_a as compared with the SEBAL model, in both stations (EC and KZL). In general, SEBAL underestimated daily ET_a for the understudied growing season within the validation footprint (Figure 6).

Daily actual ET_a in both sites ranges from 0.00 mm d⁻¹ to 6.89 mm d⁻¹ for the understudied growing season. The highest ET_a was observed on DOY 180 in the desert, and DOY 189 in the oasis, which marked the peak of summer-warmth. The day with the lowest ET_a in both sites was observed on DOY 301 (Figure 6). Note that ET_a estimates

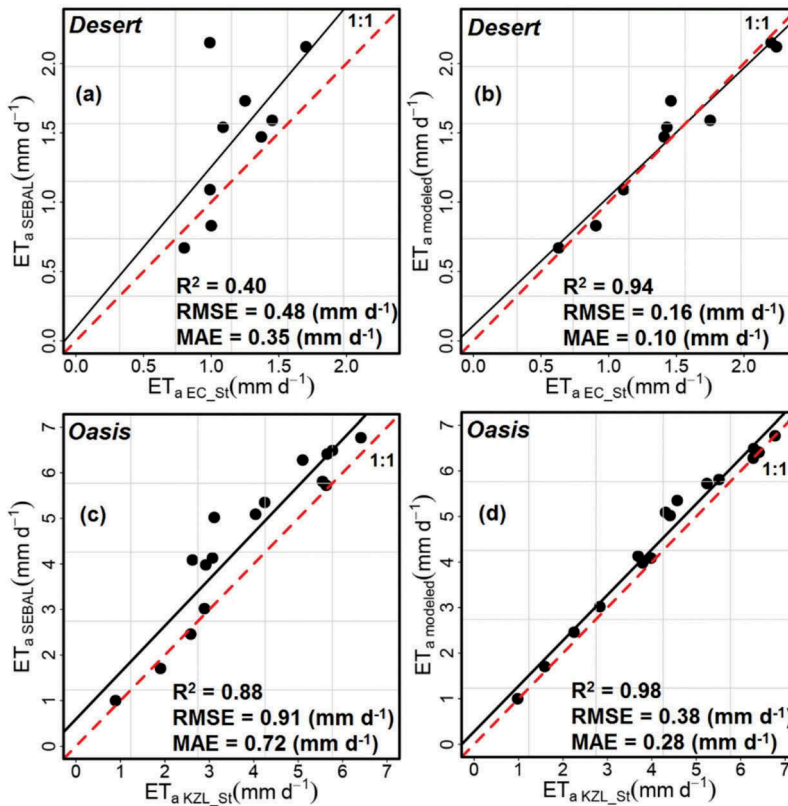


Figure 5. Comparison of high resolution derived daily ET_a estimates between ET_a observation estimates at both the EC and KZL sites. (a-b) represent the validation at the EC flux site (desert grassland) while (c-d) is the validation at the KZL site (oasis).

for the sampled days in this study may vary with those estimated from empirical water balance models for the entire Aral Sea basin (Micklin, Aladin, and Plotnikov 2014). This is explained by the inhomogeneity of the land surfaces in the region (Meng *et al.* 2017). In other words, daily ET_a estimates across land cover types in the study area vary significantly.

3.3 Dynamics of daily et_a according to land use types across the SASB

3.3.1 EC site (desert ecosystem)

As earlier established, the retrieved ET_a from the automated SEBAL model differs appreciably at both sites, according to land use types. At the EC site, on DOY 180, the highest ET_a values correspond to water bodies of the sampled portion of the SAS and the lake Kamyshlybas (Figure 1). This is followed by patches of Oasis (irrigated, non-irrigated arable and farmlands) located near these waterbodies (Figures 7 and 9). Note the difference in DOY with highest ET_a for the validation fetch area and across the basin (Figures 6 and 7).

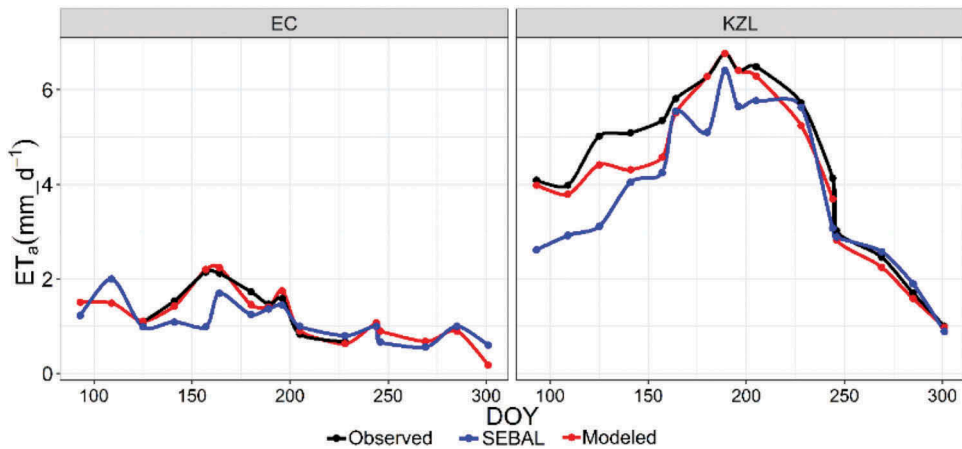


Figure 6. A model comparison of daily actual ET estimates between ground-based observation and SEBAL estimates within a 450 m² station observation fetch area.

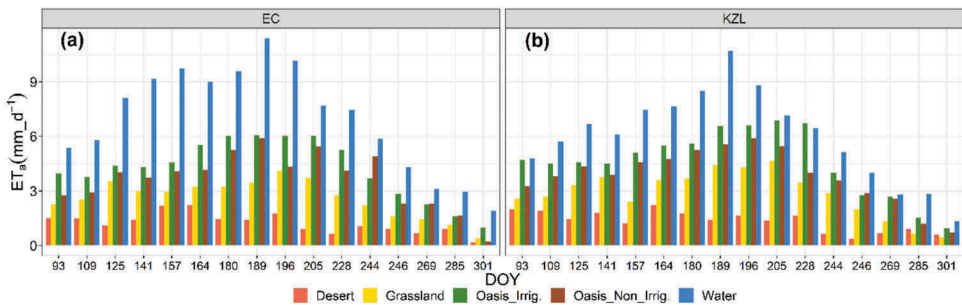


Figure 7. Growing season daily ET_a over different land cover types (a) EC site and (b) KZL site.

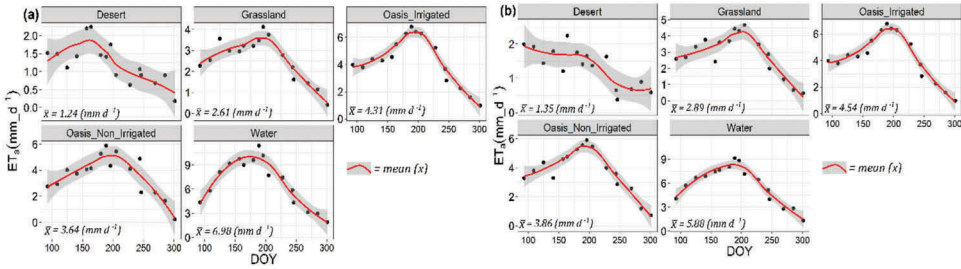


Figure 8. Daily mean estimates of ET_a at the (a) EC site and (b) KZL site.

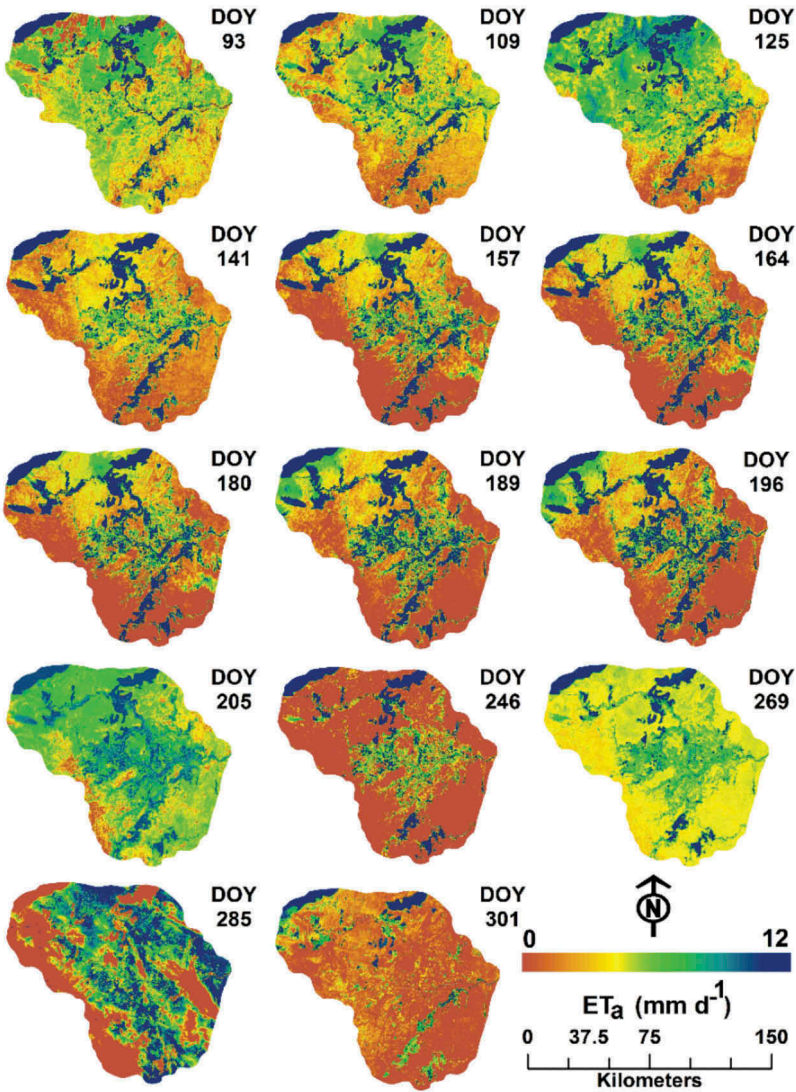


Figure 9. Spatial distribution of daily ET_a across the SASB based on $SEBAL_{auto}$ simulation.

3.3.2 KZL site (oasis ecosystem)

Also, in the Delta-dominated oasis site of the SASB, the highest ET_a corresponded with waterbodies on DOY 189. Next to water bodies are the irrigated land cover types on DOY 205, followed by non-irrigated land on DOY 196, grasslands on DOY 205 and desert surfaces on DOY 164 (Figure 7b). The dynamics of ET_a in the Oasis differ significantly from the pattern in the desert ecosystem. This can be attributed to the well-watered oasis environment that is well drained by the Syr Darya river almost throughout the year (Micklin, Aladin, and Plotnikov 2014); accounting for the high agrometeorological potential of this section of the basin for crop cultivation.

Desert grasslands recorded high ET_a estimates on DOY 196 which was still in Summer of the growing season. Previous studies have shown that normal transpiration occurs with well-vegetated areas around the Aral Sea basin, including the Small Aral Sea (Micklin, Aladin, and Plotnikov 2014; Li et al. 2011a). Which means, daily ET_a in the SASB increases with vegetation growth despite the low soil moisture induced by encroaching desert sands and will recede as vegetation decreases during summer and harvest periods. Therefore, the lowest ET_a values match with desert ecosystems and other bare surfaces, due to lower fractional vegetation cover and reduced soil moisture content. Figure 8 shows the daily estimated average ET_a values for each land cover type within the oasis and desert ecosystems.

Despite the DOY in the growing season, the average estimates of ET_a in open or bare desert surfaces were 1.24 mm d^{-1} , while in desert grasslands land cover, the average ET_a estimate was 2.61 mm d^{-1} . Average ET_a of 3.64 mm d^{-1} and 4.31 mm d^{-1} were retrieved from the non-irrigated oasis and irrigated oasis, respectively; thereby indicating a difference of about 0.67 mm d^{-1} . As noted earlier, sea surface evaporation consumes the largest, with about 6.98 mm d^{-1} in water bodies located within the desert ecosystems (Figure 8a). Average estimates of ET_a in the open desert surface was 1.34 mm d^{-1} while in the desert grasslands it was 2.89 mm d^{-1} . Non-irrigated oasis also maintained an average mean ET_a of 3.86 mm d^{-1} , while irrigated oasis recorded 4.54 mm d^{-1} . Evaporation rate in the open water surfaces is about 5.89 mm d^{-1} in the oasis ecosystem (Figure 8b). In both sites, land use ET_a estimates vary due to the different ecosystem types and the dominant land use activities. Though energy transfer and conversion largely depend on sensible heat exchange, however, for the period understudied, desert ecosystems have the lowest energy conversion rates than other land covers. During winter of the same period, energy transfer was generally low in all land cover types in both ecosystems, due to reduced incoming shortwave trapped by high humidity. Therefore, amounting to short R_n which could not produce enough energy for other flux components. Therefore, the air temperature was comparatively low, and the ice liquefaction process over glacier surfaces truncated heat transfer from DOY 269 to DOY 301.

3.4 Spatial variability of daily and monthly et_a over the SASB

The spatial pattern of ET_a over the growing season are varied and complex. Fundamentally, the growing season starts from late March-May to late September – early October (Spring-Summer-Autumn). Figure 9 illustrates the daily spatial distribution of the SEBALauto-model derived ET_a , spanning through the entire growing season over the SASB. The beginning of the growing season is signified by a relatively even distribution of daily ET_a as indicated by

the lush green background on DOY 93 (Figure 9) in both oasis and desert-grassland ecosystem and across the entire basin. On this day, ET_a was 1.51 mm d^{-1} and 4.01 mm d^{-1} for desert and oasis, respectively.

In Spring, April and early May, waterbodies maintained the highest ET rates while the irrigated oasis and arable lands situated beside water bodies constituted the second largest transpiring landscape. Note that SEBAL parametrization was initially designed for land (arable). However, the strong positive correlation between ET_a and E_{pan} in a previous study proves it is reliable, for at least, basin-size waterbodies (Conrad et al. 2007). The evaporating waterbodies include the east part of the SAS (top left of the basin-Figure 9), small inland lakes (e.g., lake Kamyshlybas located north of the basin) and the Syr Darya run-off channel which empties into the small Aral Sea. The run-off supports the growth of oasis and conversion of deserts through expanding irrigation activities within the basin. Daily variations of ET_a spanning through the growing season at the different sites may appear similar with some DOY (Figure 9). Nevertheless, towards the south of the basin are clear evidence of reduced evaporative fraction represented by brown desert covers on DOY 109 and DOY 125. Actual ET rates for these days range from 1.49 mm d^{-1} to 1.79 mm d^{-1} , respectively. Again, note that the highest ET_a rates are associated with waterbodies, fluctuating between 6.69 mm d^{-1} and 8.1 mm d^{-1} , with peaks in July -August (11.7 mmd^{-1}).

Summer gradually sets in from mid-May, and sometimes, extends to August. These periods are marked by high ET_a rates in the region. DOY 141 revealed that transpiration occurs more in the Oasis (irrigated and arable lands), and partly in the grasslands as indicated by the concentration of green vegetative cover in the delta of Syr Darya river, with patches of scattered green cover across the basin (Figure 9). ET_a rate for this day increased to 5 mmd^{-1} in the Oasis but reduced to 1 mmd^{-1} in the desert areas. The ET_a variability can be attributed to the irrigation concertation practices on Oasis crops (Li et al. 2014) while extreme climate conditions of low precipitation and high summer temperature, saline and alkaline soils are responsible for the reduced ET_a rates in the desert ecosystem (Li et al. 2011a). Also, on days of the year 157, 164 and 180 in June, high ET_a rates appear concentrated in the oasis than in the surrounding deserts. During this period of the growing season, and also in July (DOY 189, 196 and 205) oasis crop fields receive more irrigated water, which increases soil texture and crop water holding capacity. Thereby enhancing root water uptake, resulting in more soil evaporation and plant transpiration, with less significant effect in the desert grassland and other bare surfaces. Daily ET_a rates for the days in June range from 4.07 to 6.28 mm d^{-1} in the Oasis, and 1.46 mm d^{-1} to 2.46 mm d^{-1} in the desert ecosystem; but are much higher in July-August, oasis: 6.41 to 6.77 mm d^{-1} , and lower in the desert: 0.90 mm d^{-1} to 1.74 mm d^{-1} . These results are somewhat different from a comparable basin experiment performed by Conrad et al. (2007) in Khorezm oblast (located in the lower reaches of the Amur Darya river) within the larger Aral Sea basin. Their study shows that early in July, ET_a is usually low (1.04 mm), unlike in the SASB. This may have resulted from weak transpiration of less irrigated crops; however, during intense irrigation stages (late June – September), ET_a rates are high in Summer (Conrad et al. 2007).

Figure 10 shows the SEBAL_{auto} derived monthly ET_a and season ET_a spatial distribution across the SASB. There exists substantial evidence of basin-scale variations and regional gradients of monthly ET_a with north-southward decreasing trends. Monthly ET_a was generally low in the south than in the north of the understudied basin, whereas

comparatively high estimates were concentrated in the delta dominated oasis, due to the Syr Darya run-off into the upper (small) Aral Sea. However, in September and October, there was a clear indication of low ET_a distribution. Suggesting that the spatial distribution of monthly ET_a correlates strongly with season timing, especially in Autumn and Winter. Note that August was omitted because of inconsistent Landsat footprint paths earlier discussed in [section 2.2.2](#). For this reason, spatially distributed daily (DOY 228 and 244) and aggregated monthly ET_a for August were excluded but was captured in the daily ET_a validation, and therefore, their ET_a rates were captured in the season ET estimation ([Figure 10b](#)). The $SEBAL_{auto}$ -modeled monthly ET_a indicates uniformly average ET_a estimates in April with relatively low estimates toward the SAS lake-surrounded desert grasslands in the north. In May, ET_a distribution was moderately high around waterbodies and oasis but was low in the desert south of the basin. Precipitation is generally low in this region but may have been evident in April and May (Micklin, Aladin, and Plotnikov 2014). In Summer (June-July), irrigation activities were intensified, with high NDVI. Therefore, while the desert areas appeared completely dry with low soil moisture content, crop-fields and well-watered lands were contributing the most to high ET_a estimates.

In June, higher ET_a values were associated with waterbodies, while in July both oasis and waterbodies maintain high ET_a . Mid-July has the highest ET_a rates in this basin, as indicated by summer ET_{ins} ([Figure 11](#)).

This is due to the supporting Syr Darya run-off, that is consistent almost throughout the year, unlike the ephemeral Amur Darya river (Micklin, Aladin, and Plotnikov 2014). Secondly, the rates of increased irrigation activities and expanding oasis during this period also influenced ET_a rates. In August, the ET_a reduced due to harvest and low vegetation index. September and October are considered as winter months with truncated R_n which weakens heat transfer that produces low energy and the slow melting process of glaciers and low air temperature.

[Figure 10b](#) shows the season ET_a cumulatively calculated for DOY 93–301 from the $SEBAL_{auto}$ simulation. The growing season ET_a for land surfaces ranges between 658 – < 850 mm. The value represents the total seasonal water use for the understudied basin, but with significantly high values from the open water bodies of the SAS, inner lakes and Syr Darya run-off. An earlier study conducted within the region, in Khorezm, estimated

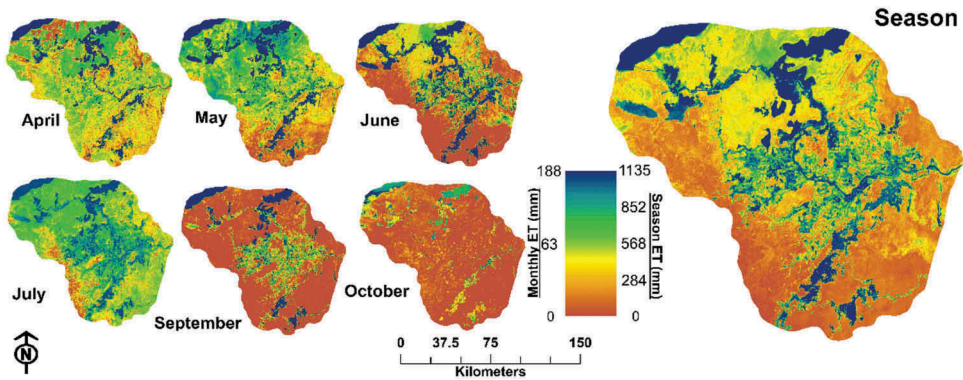


Figure 10. (a) Monthly spatial distribution of ET_a variability, and (b) season ET_a distribution across the Small Aral Sea Basin based on $SEBAL_{auto}$ simulation.

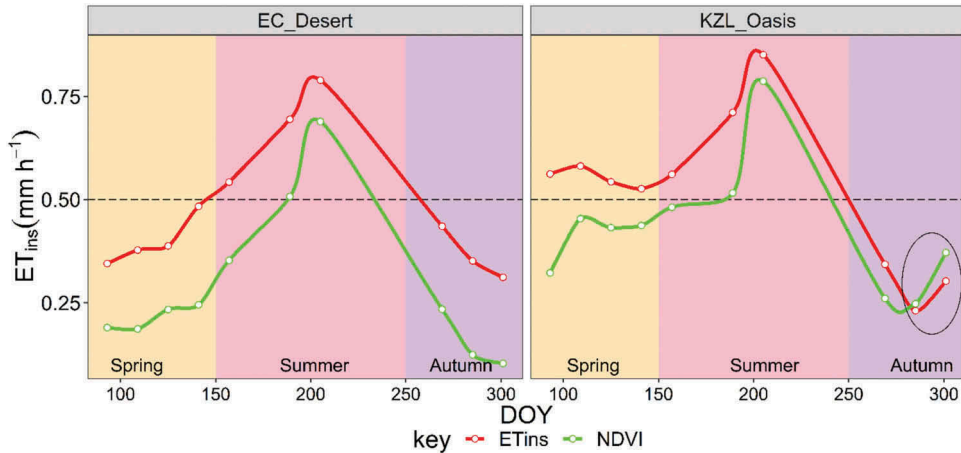


Figure 11. The daily pattern of landscape evaporative demand based on NDVI and ET_{ins} in the desert and oasis ecosystems of the SASB. The demarcated black dash lines indicate the high and low variability of ET_{ins} -NDVI ratio. The black circled line in the Autumn at the KZL site indicate the interception of transpiration by a peculiar local winter advection effect.

season ET_a values to be larger than 1200mm (Conrad et al. 2007). Nevertheless, overall pan evaporation for the area could reach up to 1546 mm, which is higher than the total annual precipitation (Li et al. 2011a). Following the Land cover classes (Figure 1b), the season ET distribution indicate that irrigated oasis consumes and transpires more water than other land cover types, beside waterbodies. While desert land cover consumes less water during the growing season (Figure 10b). Otherwise, the total season ET_a for the SASB could reach up to 1135 mm with the inclusion of evaporation from water bodies (Figure 10b). Here, we see that high-resolution Landsat 7 ETM+ simulation is a reliable approach for extracting land cover water consumption rates, and even beyond in-between seasonal timescale in the heterogeneous SASB.

3.5 ET response to canopy density and water stress conditions in the desert and oasis ecosystems

A comparative assessment of vegetation photosynthetic response, evident in the analogous NDVI- ET_{ins} relationship in the oasis-desert ecosystem is shown in Figure 11. The SEB approach applied to the flora component suggests a linear relationship of T_s change between vegetation and canopy air stream, which also controls transpiration (Boegh et al. 1999). However, due to the gradual onset of winter snow, canopy conductance from the slope coefficient of the NDVI- ET_{ins} relationship indicated low stomatal sensitivity to atmospheric-vapor pressure shortage between DOY 285–301. As a result, surface transpiration was truncated in late-autumn at the KZL site during those DOY (Figure 11). Which means that the water stress situation in the oasis-desert ecosystem is instead, conditioned more by energy availability than stomatal conductance.

Nevertheless, in the SASB, ET_{ins} fluctuates with increasing (decreasing) NDVI trends and is directly proportional to canopy density (Li et al. 2011a). Though the region recurrently experiences warming, however, most parts have been greening. Over 55% of the study region has experienced significant variations in the rate of change in NDVI

(Yuan *et al.* 2017). The strength of ET_{ins} trends strongly correlates with NDVI trends to infer on the influence of warming by rising surface air temperature in the SASB. Therefore, terrestrial vapor fluxes in semi-arid and arid areas are primarily influenced by plant transpiration upon the availability of energy.

Despite that NDVI trends can suppress temperature effects due to alterations of surface energy (late-Autumn in Oasis, Figure 12), landscape greenness still plays an important function in the intensification of terrestrial ET. In the desert ecosystem (Spring – DOY 93, 109, 125 and 141), NDVI ratio was < 0.25 , while the rates of ET_{ins} were generally higher than this estimate. However, in the oasis ecosystem, for the same period, NDVI rates were much higher than those of the desert ecosystem ($0.32 < 0.44$), with corresponding ET_{ins} range (0.60 mm h^{-1} – 0.72 mm h^{-1}). Therefore, desert and oasis consumptive water use varies significantly with the time of the season but are much higher in summer than in other periods (Figure 11). However, the evaporative demand in oasis remains higher than in the desert ecosystem. Most importantly, regarding spatial dynamics, the growing season spatial variation of modeled ET_{ins} to NDVI ratio show that surface heterogeneity at both sites contrast but contribute distinctly to basin-wide evaporative demand.

The varying impact of land use activities at a specific time of the season significantly determines the surface area ecological changes that control transpiration rates. Similarly, the sensitivity of localized climate to vegetation variations, as typified by NDVI in dry regions does have an enormous impact on dryland water resources (Jiang, Liang, and Yuan 2015). For instance, between DOY 93 – DOY 141 (mid- to late-spring) at both sites, precipitation was still evident and was signified by a negative correlation with T_s . However, a peculiar pattern was observed on DOY 125, which revealed the ET-induced cooling effect in the desert ecosystem than in the Oasis (Figure 12). This resulted because additional energy dissipated via ET_{ins} was less than the energy absorbed by albedo.

Our finding agrees with the postulations of Yuan *et al.* (2017), that when the quantity of absorbed energy by albedo exceed dissipation through evapotranspiration, a heating effect is likely to manifest. This hypothesis contrast with the observation on DOY 125 in the desert ecosystem but are valid for other days of the year (Figure 12). Another critical finding was exhibited in October, particularly on DOY 301. Desert landscapes were superficially covered with winter snow, to erroneously present high spatially distributed ET or ET_{ins} -NDVI ratio (Figure 12). However, Figure 11 shows the accurate representation of NDVI and ET_{ins} on DOY 301 of the growing season for desert ecosystem (NDVI – 0.11 and ET_{ins} – 0.31 mm h^{-1}) and oasis ecosystem (NDVI – 0.37 and ET_{ins} – 0.303 mm h^{-1}). This gives the reason for the seemingly different spatial distribution of ET_{ins} in different times of the growing season as illustrated by the daily spatial distribution maps (Figures 9, 10 and 12).

3.6 Uncertainties

The automated calibration of Landsat 7 ETM+ endmember pixels in SEBAL comparatively produced high accuracies (R^2) for energy fluxes and ET_a in this study (Table 2, Figure 5). However, it is unlikely that the complexity of the region will guarantee consistent application in other parts of the larger Aral Sea basin with higher elevations. This problem can be handled by correcting for the lapsed difference in T_s , which if left uncorrected, can result in orographic effects (Allen *et al.* 2001). Secondly, the use of coarse resolution datasets or poorly corrected energy balance closure may amount to a varying degree of discrepancies.

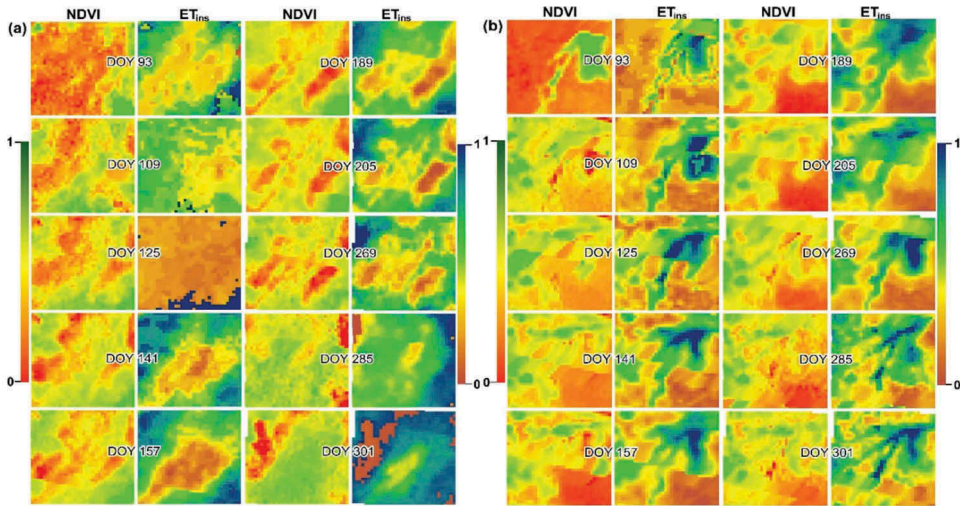


Figure 12. Daily spatial variations of ET_{ins} response to vegetation index and landscape evaporative demand at both sites. (a) show the pattern in the EC flux fetch area, while (b) shows the pattern in the KZL station fetch area. The EC site is relatively dominated by desert grassland while the KZL site consists mostly of irrigated and non-irrigated arable land cover.

Thirdly, though the study area lacks adequate observational data, and that the study was based on a comprehensive mapping of a growing season surface energy and vapor fluxes, however, inter-seasonal comparison beyond one growing season may provide a better assessment of the model to guide future research. Note that ET_a variability over land cover types across the basin may appear somewhat similar (differ) in some instances because the validation was performed within a 450 m^2 flux system and meteorological station fetch areas, and not for all part of the basin. Therefore, error sources in ET estimation can arise from numerous factors and may require further investigation. For instance, limitation in the relationship between R_n and soil moisture content in winter can result in erroneous predictive models (Mallick et al. 2018).

4 Conclusion

This article demonstrates the reliability of high-resolution satellite-driven surface energy balance modeling of surface energy fluxes across a heterogenous basin, even with the paucity of observational data. Also, the study improves on the estimation of vapor flux by characterizing the role of different land use types to ET variability in the SASB. First, the accuracy range for the energy balance ratio was reasonable (77 to 100%). Then, the meteorological and flux tower validations returned high accuracies (high R^2 , low RMSE and low MAE), indicating that the automated SEBAL model is more stable and capable of predicting surface energy and vapor fluxes over the complex SASB. The responses of ET to land use types differ characteristically in desert and oasis ecosystems. Beside water bodies (particularly, SAS), irrigated oasis accounted for the highest ET rates, and was heightened in summer due to intensive irrigation practices; while desert grasslands correspond to low ET rates across the growing season. Apart from limited precipitation and the general increase in surface air temperature, other controlling factors of ET

variability in the SASB include ET-induced oasis-desert effects arising from increased land use activities, mainly, irrigation expansion towards desert areas. Second is the north-south directional effects of vegetation changes on local temperature gradients, which occasionally leads to decreased temperature due to increased ET rates (mainly in the oasis), and vice versa (in the desert). Moreover, the ET_{ins} -NDVI ratio indicates that ET changes strongly correlates with canopy density across the entire basin, but with uncertainties in late-autumn and winter. In other words, inadequate observation data constrained the accurate estimation of ET rates in Winter (November to March); hence, the limitation of the study. Future studies can explore and evaluate the potential of an only satellite-based derivation of ET information, which has proven reliable over similar areas, to complement gaps in ground observation data. Particularly, long-term assessment is needful to further describe the impacts of extreme climatic events on interseasonal and interannual ET responses to future land process dynamics in the Aral Sea basin. Finally, this study provides the essential ET framework and baseline information for SASB that may be useful for such long-term studies that will guide in agrometeorological services and sustainable management of water resources in arid regions.

Highlights

- A comprehensive investigation of a growing season dynamics of near-surface and vapor fluxes is presented.
- ET_a variability over land cover types vary significantly and are primarily influenced by dominant advection effects in the oasis and desert ecosystems
- Extra energy dissipated by ET_{ins} was less than the energy absorbed by albedo in SASB
- ET in SASB is directly proportional to canopy density

Acknowledgements

The United States Geological Survey (<http://earthexplorer.usgs.gov>) is gratefully acknowledged for providing the Landsat 7 ETM+ (GeoTIFF) images at no cost. Thanks to Dr. Yuan Xiuliang who made available the EC flux tower data used in this study, the reviewing editor(s) and all the reviewers for their suggestions that helped to improve the paper. We acknowledge the supports received from the Strategic Priority Research Program of Chinese Academy of Sciences (Grant No. XDA20060302), the National Natural Science Foundation of China (Grant No. U1803243), the West Light Foundation of The Chinese Academy of Sciences (2018-XBQNXZ-B-011), and the Chinese Academy of Sciences-the World Academy of Sciences (CAS-TWAS) President's Fellowship Programme (2017A8010210001).

Disclosure statement

No potential conflict of interest was reported by the authors.

Funding

This work was supported by Strategic Priority Research Program of Chinese Academy of Sciences [Grant No. XDA20060302]; National Natural Science Foundation of China [Grant No. U1803243]; West Light Foundation of the Chinese Academy of Sciences [2018-XBQNXZ-B-011]; The Chinese Academy of Sciences-the World Academy of Sciences (CAS-TWAS) President's Fellowship Programme [2017A8010210001]

ORCID

Friday Uchenna Ochege  <http://orcid.org/0000-0002-6661-0966>

Geping Luo  <http://orcid.org/0000-0003-0553-9454>

George Owusu  <http://orcid.org/0000-0003-2518-6676>

Eldiir Duulatov  <http://orcid.org/0000-0001-5978-2762>

Liangzhong Cao  <http://orcid.org/0000-0002-1686-6998>

Jean Baptiste Nsengiyumva  <http://orcid.org/0000-0002-0295-2094>

References

- Al Zayed, I. S., N. A. Elagib, L. Ribbe, and J. Heinrich. 2016. "Satellite-based Evapotranspiration over Gezira Irrigation Scheme, Sudan: A Comparative Study." *Agricultural Water Management* 177: 66–76. doi:10.1016/j.agwat.2016.06.027.
- Allen, R., A. Irmak, R. Trezza, J. M. Hendrickx, W. Bastiaanssen, and J. Kjaersgaard. 2011. "Satellite-based ET Estimation in Agriculture Using SEBAL and METRIC." *Hydrological Processes* 25: 4011–4027. doi:10.1002/hyp.8408.
- Allen, R., A. Morse, M. Tasumi, W. Bastiaanssen, W. Kramber, and H. Anderson. 2001. "Evapotranspiration from Landsat (SEBAL) for Water Rights Management and Compliance with Multi-state Water Compacts." Paper read at Geoscience and Remote Sensing Symposium, 2001. IGARSS'01. IEEE 2001 International, Sydney, NSW, Australia. doi:10.1109/IGARSS.2001.976651.
- Allen, R., M. Tasumi, R. S. TREZZA, and W. Bastiaanssen. 2002. "Surface Energy Balance Algorithm for Land: Advanced Training and Users Manual." In *Idaho: [sn]*.
- Allen, R. G., B. Burnett, W. Kramber, J. Huntington, J. Kjaersgaard, A. Kilic, C. Kelly, and R. Trezza. 2013. "Automated Calibration of the Metric-Landsat Evapotranspiration Process." *Journal of the American Water Resources Association (JAWRA)* 49 (3). doi:10.1111/jawr.12056.
- Allen, R. G., W. O. Pruitt, J. L. Wright, T. A. Howell, F. Ventura, R. Snyder, D. Itenfisu, P. Steduto, J. Berengena, and J. B. Yrisarry. 2006. "A Recommendation on Standardized Surface Resistance for Hourly Calculation of Reference ETo by the FAO56 Penman-Monteith Method." *Agricultural Water Management* 81 (1–2): 1–22. doi:10.1016/j.agwat.2005.03.007.
- Bastiaanssen, W., E. Noordman, H. Pelgrum, G. Davids, B. Thoreson, and R. Allen. 2005. "SEBAL Model with Remotely Sensed Data to Improve Water-resources Management under Actual Field Conditions." *Journal of Irrigation and Drainage Engineering* 131 (1): 85–93. doi:10.1061/(ASCE)0733-9437(2005)131:1(85).
- Bastiaanssen, W. G., M. F. Menenti, and A. R. A. Holtslag. 1998a. "A Remote Sensing Surface Energy Balance Algorithm for Land (SEBAL). 1. Formulation." *Journal of Hydrology* 212: 198–212. doi:10.1016/S0022-1694(98)00253-4.
- Bastiaanssen, W. G., H. Pelgrum, J. Wang, Y. Ma, J. Moreno, G. Roerink, and T. Van der Wal. 1998b. "A Remote Sensing Surface Energy Balance Algorithm for Land (SEBAL).: Part 2: Validation." *Journal of Hydrology* 212: 213–229. doi:10.1016/S0022-1694(98)00254-6.
- Bhattarai, N., and T. Liu. 2019. "LandMOD ET Mapper: A New Matlab-based Graphical User Interface (GUI) for Automated Implementation of SEBAL and METRIC Models in Thermal Imagery." *Environmental Modelling & Software* 118: 76–82. doi:10.1016/j.envsoft.2019.04.007.
- Bhattarai, N., K. Mallick, J. Stuart, B. D. Vishwakarma, R. Niraula, S. Sen, and M. Jain. 2019. "An Automated Multi-model Evapotranspiration Mapping Framework Using Remotely Sensed and Reanalysis Data." *Remote Sensing of Environment* 229: 69–92. doi:10.1016/j.rse.2019.04.026.
- Bhattarai, N., L. J. Quackenbush, J. Im, and S. B. Shaw. 2017. "A New Optimized Algorithm for Automating Endmember Pixel Selection in the SEBAL and METRIC Models." *Remote Sensing of Environment* 196: 178–192. doi:10.1016/j.rse.2017.05.009.
- Biggs, T. W., M. Marshall, and A. Messina. 2016. "Mapping Daily and Seasonal Evapotranspiration from Irrigated Crops Using Global Climate Grids and Satellite Imagery:

- Automation and Methods Comparison.” *Water Resources Research* 52. doi:10.1002/2016WR019107.
- Boegh, E., H. Sogaard, N. Hanan, P. Kabat, and L. Lesch. 1999. “A Remote Sensing Study of the NDVI-Ts Relationship and the Transpiration from Sparse Vegetation in the Sahel Based on High-resolution Satellite Data.” *Remote Sensing of Environment* 69 (3): 224–240. doi:10.1016/S0034-4257(99)00025-5.
- Brutsaert, W. 1999. “Aspects of Bulk Atmospheric Boundary Layer Similarity under Free Convective Conditions.” *Reviews of Geophysics* 37 (4): 439–451. doi:10.1029/1999RG900013.
- Choi, M., W. P. Kustas, M. C. Anderson, R. G. Allen, F. Li, and J. H. Kjaersgaard. 2009. “An Intercomparison of Three Remote Sensing-based Surface Energy Balance Algorithms over a Corn and Soybean Production Region (Iowa, US) during SMACEX.” *Agricultural and Forest Meteorology* 149 (12): 2082–2097. doi:10.1016/j.agrformet.2009.07.002.
- Conrad, C., S. W. Dech, M. Hafeez, J. Lamers, C. Martius, and G. Strunz. 2007. “Mapping and Assessing Water Use in a Central Asian Irrigation System by Utilizing MODIS Remote Sensing Products.” *Irrigation Drainage System* 21: 197–218. doi:10.1007/s10795-007-9029-z.
- Cuenca, R. H., S. P. Ciotti, and Y. Hagimoto. 2013. “Application of Landsat to Evaluate Effects of Irrigation Forbearance.” *Remote Sensing* 5: 3776–3802. doi:10.3390/rs5083776.
- Gao, Z., Q. Wang, X. Cao, and W. Gao. 2014. “The Responses of Vegetation Water Content (EWT) and Assessment of Drought Monitoring along a Coastal Region Using Remote Sensing.” *GIScience & Remote Sensing* 51 (1): 1–16. doi:10.1080/15481603.2014.882564.
- Gong, T., H. Lei, D. Yang, Y. Jiao, and H. Yang. 2017. “Monitoring the Variations of Evapotranspiration Due to Land Use/Cover Change in a Semiarid Shrubland.” *Hydrology and Earth System Sciences* 21 (2): 863–877. doi:10.5194/hess-21-863-2017.
- Gowda, P. H., J. L. Chavez, P. D. Colaizzi, S. R. Evett, T. A. Howell, and J. A. Tolck. 2008. “ET Mapping for Agricultural Water Management: Present Status and Challenges.” *Irrigation Science* 26 (2): 223–237. doi:10.1007/s00271-007-0088-6.
- Grosso, C., G. Manoli, M. Martello, Y. Chemin, D. Pons, P. Teatini, I. Piccoli, and F. Morari. 2018. “Mapping Maize Evapotranspiration at Field Scale Using SEBAL: A Comparison with the FAO Method and Soil-Plant Model Simulations.” *Remote Sensing* 10 (9): 1452. doi:10.3390/rs10091452.
- He, R., Y. Jin, M. M. Kandelous, D. Zaccaria, B. L. Sanden, R. L. Snyder, J. Jiang, and J. W. Hopmans. 2017. “Evapotranspiration Estimate over an Almond Orchard Using Landsat Satellite Observations.” *Remote Sensing* 9 (5): 436. doi:10.3390/rs9050436.
- Hong, S.-H., J. M. Hendrickx, and B. Borchers. 2009. “Up-scaling of SEBAL Derived Evapotranspiration Maps from Landsat (30 M) to MODIS (250 M) Scale.” *Journal of Hydrology* 370 (1–4): 122–138. doi:10.1016/j.jhydrol.2009.03.002.
- Jaafar, H. H., and F. A. Ahmad. 2019. “Time Series Trends of Landsat-based ET Using Automated Calibration in METRIC and SEBAL: The Bekaa Valley, Lebanon.” *Remote Sensing of Environment*. doi:10.1016/j.rse.2018.12.033.
- Jiang, B., S. Liang, and W. Yuan. 2015. “Observational Evidence for Impacts of Vegetation Change on Local Surface Climate over Northern China Using the Granger Causality Test.” *Journal of Geophysical Research: Biogeosciences* 120 (1): 1–12. doi:10.1002/2014JG002741.
- Jiang, Y., and Q. Weng. 2017. “Estimation of Hourly and Daily Evapotranspiration and Soil Moisture Using Downscaled LST over Various Urban Surfaces.” *GIScience & Remote Sensing* 54 (1): 95–117. doi:10.1080/15481603.2016.1258971.
- Jiménez Bello, M. A., J. R. Castel, L. Testi, and D. S. Intrigliolo. 2015. “Assessment of a Remote Sensing Energy Balance Methodology (SEBAL) Using Different Interpolation Methods to Determine Evapotranspiration in a Citrus Orchard.” Paper read at IEEE Journal of Selected Topics in Applied Earth Observations and Remote Sensing. doi:10.1109/JSTARS.2015.2418817.
- Karimi, P., and W. G. Bastiaanssen. 2015. “Spatial Evapotranspiration, Rainfall and Land Use Data in Water Accounting—Part 1: Review of the Accuracy of the Remote Sensing Data.” *Hydrology and Earth System Sciences* 19 (1): 507–532. doi:10.5194/hess-19-507-2015.
- Kong, J., Y. Hu, L. Yang, Z. Shan, and Y. Wang. 2018. “Estimation of Evapotranspiration for the Blown-sand Region in the Ordos Basin Based on the SEBAL Model.” *International Journal of Remote Sensing*. doi:10.1080/01431161.2018.1508919.
- Kostianoy, A. G., and A. N. Kosarev, eds. 2010. *The-Aral-Sea-Environment*. Berlin Heidelberg: Springer Verlag. doi:10.1007/978-3-540-88277-0.
- Landsat Handbook. 2007. *Landsat 7 Science Data Users Handbook*. USA: NASA.

- Lee, Y., and S. Kim. 2016. "The Modified SEBAL for Mapping Daily Spatial Evapotranspiration of South Korea Using Three Flux Towers and Terra MODIS Data." *Remote Sensing* 8 (983). doi:10.3390/rs8120983.
- Li, L., X. Chen, C. V. D. Tol, G. Luo, and Z. Su. 2014. "Growing Season Net Ecosystem CO₂ Exchange of Two Desert Ecosystems with Alkaline Soils in Kazakhstan." *Ecology and Evolution* 4 (1): 14–26. doi:10.1002/ece3.910.
- Li, L., G. Luo, X. Chen, Y. Li, G. Xu, H. Xu, and J. Bai. 2011a. "Modelling Evapotranspiration in a Central Asian Desert Ecosystem." *Ecological Modelling* 222 (20–22): 3680–3691. doi:10.1016/j.ecolmodel.2011.09.002.
- Li, W., S. Lü, S. Fu, X. Meng, and H. C. Nnamchi. 2011b. "Numerical Simulation of Fluxes Generated by Inhomogeneities of the Underlying Surface over the Jinta Oasis in Northwestern China." *Advances in Atmospheric Sciences* 28 (4): 887–906. doi:10.1007/s00376-010-0041-0.
- Long, D., and V. P. Singh. 2010. "Integration of the GG Model with SEBAL to Produce Time Series of Evapotranspiration of High Spatial Resolution at Watershed Scales." *Journal of Geophysical Research* 115: 1–22. doi:10.1029/2010JD014092,2010.
- Madugundu, R., K. A. Al-Gaadi, E. Tola, A. A. Hassaballa, and V. C. Patil. 2017. "Performance of the METRIC Model in Estimating Evapotranspiration Fluxes over an Irrigated Field in Saudi Arabia Using Landsat-8 Images." *Hydrology and Earth System Sciences* 21 (12): 6135–6151. doi:10.5194/hess-21-6135-2017.
- Mallick, K., E. Toivonen, I. Trebs, E. Boegh, J. Cleverly, D. Eamus, H. Koivusalo, et al. 2018. "Bridging Thermal Infrared Sensing and Physically-Based Evapotranspiration Modeling: From Theoretical Implementation to Validation across an Aridity Gradient in Australian Ecosystems." *Water Resources Research* 54 (5): 3409–3435. doi:10.1029/2017WR021357.
- Meng, X., H. Wang, Y. Wu, A. Long, J. Wang, C. Shi, and X. Ji. 2017. "Investigating Spatiotemporal Changes of the Land-surface Processes in Xinjiang Using High-resolution CLM3. 5 And CLDAS: Soil Temperature." *Scientific Reports* 7 (1): 13286. doi:10.1038/s41598-017-10665-8.
- Micklin, P. 2016. "The Future Aral Sea: Hope and Despair." *Environmental Earth Sciences* 75 (9): 844. doi:10.1007/s12665-016-5614-5.
- Micklin, P., N. V. Aladin, and I. S. Plotnikov, eds. 2014. *The Aral Sea: The Devastation and Partial Rehabilitation of a Great Lake*. edited by P. Blondel. Berlin, Heidelberg: Springer. doi:10.1007/978-3-642-02356-9.
- Mira, M., A. Olioso, B. Gallego-Elvira, D. Courault, S. Garrigues, O. Marloie, O. Hagolle, P. Guillevic, and G. Boulet. 2016. "Uncertainty Assessment of Surface Net Radiation Derived from Landsat Images." *Remote Sensing of Environment* 175: 251–270. doi:10.1016/j.rse.2015.12.054.
- Mutiga, J. K., Z. Su, and T. Woldai. 2010. "Using Satellite Remote Sensing to Assess Evapotranspiration Case Study of the Upper Ewaso Ng'iro North Basin, Kenya." *International Journal of Applied Earth Observation and Geoinformation* 12: 100–108. doi:10.1016/j.jag.2009.09.012.
- Nistor, M. M., S. Cheval, A. F. Gualtieri, A. Dumitrescu, V. E. Boțan, A. Berni, G. Hognogi, I. A. Irimuş, and C. G. Porumb-Ghiurco. 2017. "Crop Evapotranspiration Assessment under Climate Change in the Pannonian Basin during 1991–2050." *Meteorological Applications* 24 (1): 84–91. doi:10.1002/met.1607.
- Ortega-Farias, S., and R. López-Olivari. 2010. "Evaluation of a Two-layer Model to Estimate the Latent Heat Flux over a Drip-Irrigated Olive Orchard." Paper read at 5th National Decennial Irrigation Conference Proceedings, 5-8 December 2010, Phoenix Convention Center, Phoenix, Arizona USA, at St. Joseph, MI. doi:10.13031/2013.35824.
- Owusu, G. 2017. "Sebkc: Surface Energy Balance and Crop Coefficient Estimation with R. Github." <https://github.com/gowusu/sebkc>
- Silva Oliveira, B., E. Caria Moraes, M. Carrasco-Benavides, G. Bertani, and G. Augusto Verola Mataveli. 2018. "Improved Albedo Estimates Implemented in the METRIC Model for Modeling Energy Balance Fluxes and Evapotranspiration over Agricultural and Natural Areas in the Brazilian Cerrado." *Remote Sensing* 10 (8): 1181. doi:10.3390/rs10081181.
- Singh, A., A. Behrang, J. B. Fisher, and J. T. Reager. 2018. "On the Desiccation of the South Aral Sea Observed from Spaceborne Missions." *Remote Sensing* 10 (793). doi:10.3390/rs10050793.

- Song, L., S. Liu, W. P. Kustas, J. Zhou, Z. Xu, T. Xia, and M. Li. 2016. "Application of Remote Sensing-based Two-source Energy Balance Model for Mapping Field Surface Fluxes with Composite and Component Surface Temperatures." *Agricultural and Forest Meteorology* 230-231: 8–19. doi:10.1016/j.agrformet.2016.01.005.
- Sur, C., S. Kang, J.-S. Kim, and M. Choi. 2015. "Remote Sensing-based Evapotranspiration Algorithm: A Case Study of All Sky Conditions on a Regional Scale." *GIScience & Remote Sensing* 52 (5): 627–642. doi:10.1080/15481603.2015.1056288.
- Tang, R., Z.-L. Li, K.-S. Chen, Y. Jia, C. Li, and X. Sun. 2013. "Spatial-scale Effect on the SEBAL Model for Evapotranspiration Estimation Using Remote Sensing Data." *Agricultural and Forest Meteorology* 174: 28–42. doi:10.1016/j.agrformet.2013.01.008.
- Timmermans, W. J., W. P. Kustas, M. C. Anderson, and A. N. French. 2007. "An Intercomparison of the Surface Energy Balance Algorithm for Land (SEBAL) and the Two-source Energy Balance (TSEB) Modeling Schemes." *Remote Sensing of Environment* 108 (4): 369–384. doi:10.1016/j.rse.2006.11.028.
- Wang, C., J. Yang, S. W. Myint, Z.-H. Wang, and B. Tong. 2016. "Empirical Modeling and Spatio-temporal Patterns of Urban Evapotranspiration for the Phoenix Metropolitan Area, Arizona." *GIScience & Remote Sensing* 53 (6): 778–792. doi:10.1080/15481603.2016.1243399.
- Wang, K., and R. E. Dickinson. 2012. "A Review of Global Terrestrial Evapotranspiration: Observation, Modeling, Climatology, and Climatic Variability." *Reviews of Geophysics* 50 (2). doi:10.1029/2011RG000373.
- Yan, N., F. Tian, B. Wu, W. Zhu, and M. Yu. 2018. "Spatiotemporal Analysis of Actual Evapotranspiration and Its Causes in the Hai Basin." *Remote Sensing* 10 (2): 332. doi:10.3390/rs10020332.
- Yang, Y., Y. Yang, D. Liu, T. Nordblom, B. Wu, and N. Yan. 2014. "Regional Water Balance Based on Remotely Sensed Evapotranspiration and Irrigation: An Assessment of the Haihe Plain, China." *Remote Sensing* 6 (3): 2514–2533. doi:10.3390/rs6032514.
- Yang, Y., X. Zhou, Y. Yang, S. Bi, X. Yang, and D. L. Liu. 2018. "Evaluating Water-saving Efficiency of Plastic Mulching in Northwest China Using Remote Sensing and SEBAL." *Agricultural Water Management* 209: 240–248. doi:10.1016/j.agwat.2018.07.011.
- Yuan, X., W. Wang, J. Cui, F. Meng, A. Kurban, and P. De Maeyer. 2017. "Vegetation Changes and Land Surface Feedbacks Drive Shifts in Local Temperatures over Central Asia." *Scientific Reports* 7 (1). doi:10.1038/s41598-017-03432-2.
- Zhang, M., G. Luo, P. D. Maeyer, P. Cai, and A. Kurban. 2017. "Improved Atmospheric Modelling of the Oasis-Desert System in Central Asia Using WRF with Actual Satellite Products." *Remote Sensing* 9 (1273). doi:10.3390/rs9121273.